Records of Natural Products



www.acgpubs.org
ORIGINAL ARTICLE

# Quercetin-induced metabolic reprogramming in LPS-stimulated BV-2 microglia: Untargeted LC–MS metabolomic profiling with molecular docking and molecular dynamics simulations

Vahap Murat Kutluay[1*], Ahmet Avcı[2], Emine Koç[3], Mustafa Çelebier[3], Veronique Seidel[4] and Ozan Kaplan[3]

[1]Department of Pharmacognosy, Faculty of Pharmacy, Hacettepe University, 06100, Sihhiye, Ankara, Türkiye
[2]Department of Pharmaceutical Chemistry, Faculty of Pharmacy, Hacettepe University, 06100, Sihhiye, Ankara, Türkiye
[3]Department of Analytical Chemistry, Faculty of Pharmacy, Hacettepe University, 06100, Sihhiye, Ankara, Türkiye
[4]Natural Products Research Laboratory, Strathclyde Institute of Pharmacy and Biomedical Sciences, University of Strathclyde, 161 Cathedral Street, Glasgow G4 0RE, UK

**Abstract:** Neuroinflammation is characterized by microglial activation, excessive nitric oxide (NO) and reactive oxygen species (ROS) production. Although quercetin is widely reported to attenuate microglial inflammation, its accompanying metabolic adaptations remain incompletely defined. In this study, the effect of quercetin on LPS-induced BV-2 cells was examined together with quercetin-associated metabolic remodeling using an integrated experimental and in silico strategy. LPS-stimulated BV-2 cells were co-treated with quercetin (1.25–10 μM) and cell viability and NO production were quantified. Untargeted LC–MS metabolomics was conducted on the control, LPS, and LPS+quercetin groups ($n$ = 6), followed by multivariate and pathway enrichment analysis. Quercetin was found to be non-cytotoxic and to significantly reduce LPS-induced NO levels in a concentration-dependent manner. Metabolomic profiling demonstrated clear group separation, with quercetin inducing a distinct metabolic phenotype intermediate between inflamed and basal states. Differential metabolites indicated remodeling of nucleotide sugars, purine intermediates, amino acid pools, and sphingolipid-related features. Pathway analysis identified glutamate metabolism as the dominant signal, alongside nitrogen-handling routes, including the urea cycle and ammonia recycling. Complementary docking and molecular dynamics simulations targeting NADPH oxidase 2 (NOX2) supported a stable interaction with quercetin. Overall, quercetin-mediated NO suppression is coupled to coordinated redox-linked metabolic remodeling in activated microglia.

**Keywords:** Quercetin, neuroinflammation, BV-2 microglia, nitric oxide, untargeted metabolomics, molecular docking, molecular dynamics simulation

**Cite this article as:**
Kutluay et al. Quercetin-induced metabolic reprogramming in LPS-stimulated BV-2 microglia: Untargeted LC–MS metabolomic profiling with molecular docking and molecular dynamics simulations. (2026). *Records of Natural Products*, 20(6):e26033766

***Received:*** *24 March 2026*
***Revised:*** *09 June 2026*
***Accepted:*** *10 June 2026*
***Published:*** *22 June 2026*

## 1 Introduction

Neuroinflammation is an intricate process characterized by glial cell activation and the consequent release of inflammatory mediators inside the central nervous system (CNS). Chronic or dysregulated inflammation can give rise to pathological conditions such as Parkinson's disease, Alzheimer's disease (AD), multiple sclerosis, and other neurodegenerative disorders marked by extensive neuronal injury (Kamila et al., 2025). Microglia, originating from monocyte precursor cells during neurodevelopment, are the resident macrophages of the CNS, and along with astrocytes play a central role as immune sentinels in the brain, regulating inflammatory processes and monitoring changes in the neural environment. In AD, for example, the accumulation of amyloid-β (Aβ) is known to activate microglia, leading to the release of nitric oxide (NO), reactive oxygen species (ROS), and pro-inflammatory mediators that contribute to neuronal damage (Heneka et al., 2025; Kwon & Koh, 2020; Singh, 2022).

NO, generated by neuronal nitric oxide synthase (nNOS) in the brain, regulates neuronal signaling and cerebral blood flow. Its interaction with N-methyl-D-aspartate (NMDA) receptors underscores a key role in memory formation, synaptic plasticity, and neurotransmission. This dual function means that nNOS functions as both a neuroprotective

*Corresponding Author: Vahap Murat Kutluay.
Email: muratkutluay@hacettepe.edu.tr

factor and a potential contributor to neurodegenerative processes (Anwar et al., 2025).

Activated microglia represent an important alternative source of free radicals in the AD brain, as they can generate substantial amounts of ROS through activation of the nicotinamide adenine dinucleotide phosphate (NADPH) oxidase complex. NADPH oxidase–derived ROS lead to the formation of various reactive nitrogen species, including the potent oxidant peroxynitrite, thereby enhancing nitrosative stress and inducing oxidative damage, protein nitration, and the S-nitrosylation of proteins, lipids, and DNA. Accumulating evidence indicates that inducible nitric oxide synthase (iNOS) expression constitutes the major source of NO responsible for these post-translational modifications, which are likely to impair the function of multiple target proteins in AD and other neurodegenerative disorders (Akiyama et al., 2000; Heneka et al., 2025).

Quercetin (2-(3,4-dihydroxyphenyl)-3,5,7-trihydroxychromen-4-one) is a well-known flavonoid commonly found in plants, that can suppress pro-inflammatory cytokine production via inhibition of NF-κB signaling and exert neuroprotective effects by modulating mitochondrial apoptotic pathways including regulation of the Bax/Bcl-2 ratio and suppression of caspase-3 activation, cytochrome c release, and PARP-1 cleavage in the cortex and hippocampus (Khan et al., 2018). In BV-2 microglial cells, quercetin attenuates LPS- and IFN-γ-induced NO production and downregulates iNOS expression. Despite these established anti-inflammatory effects, current evidence is largely limited to cytokine profiles and transcriptional regulation (Chen et al., 2005). The broader metabolic alterations accompanying LPS-induced microglial activation—and how quercetin modulates these changes at the cellular level—remain insufficiently characterized.

Increasing evidence suggests that inflammatory activation is tightly coupled to metabolic remodeling (Cheng et al., 2021). However, the specific metabolite signatures associated with microglial inflammation and their relationship to NO production and NADPH-dependent redox processes have not been systematically defined. Metabolomics provides a comprehensive approach to capture functional metabolic states and to identify pathway-level alterations linked to inflammatory activation and therapeutic intervention (Peng et al., 2015).

In the present study, we aimed to characterize metabolite alterations induced by LPS stimulation in BV-2 microglial cells and to evaluate how quercetin modulates these changes. NO levels were quantified as a functional indicator of inflammatory activation and interpreted in relation to NADPH-dependent redox processes. Untargeted LC–MS metabolomic profiling was performed to define global metabolic shifts accompanying inflammation and its modulation by quercetin, followed by multivariate modeling and pathway enrichment analysis.

In parallel, we incorporated structure-based in silico analyses to provide complementary mechanistic context for the NADPH–redox–inflammation interface. Because NADPH-dependent enzymes and redox nodes are central to inflammatory amplification in activated microglia, molecular docking was performed against a NADPH-binding domain–containing target structure to evaluate the feasibility of quercetin engagement within a predicted binding pocket. Molecular dynamics simulations were subsequently employed to assess the stability of the docked complex and the behavior of quercetin within the active pocket. Together, this integrative strategy enables a systems-level evaluation of microglial metabolic remodeling during inflammation while providing supportive molecular-level insight relevant to NADPH-linked redox regulation.

## 2 Materials and Methods

### 2.1 Chemicals, Reagents, Cell Culture Materials

Methanol (catalog no. 1060352500), acetonitrile (catalog no. 1000292500), MTT [3-(4,5-dimethylthiazol-2-yl)-2,5-diphenyl tetrazolium bromide] (catalog no. 475989), fetal bovine serum (FBS) (catalog no. F9665), Dulbecco's Modified Eagle Medium (DMEM) (catalog no. D6429), and lipopolysaccharide (LPS) (catalog no. L4391) quercetin anhydrous (>95%, catalog no. Q4951), N-(1-naphthyl) ethylenediamine dihydrochloride (catalog no. 1.06237.0005), sulfanilamide (catalog no. 1.008035.1000), sodium nitroprusside (catalog no. 1.06541) were obtained from Sigma (St. Louis, MO, USA).

Phosphoric acid (catalog no. 1.00563), formic acid (LC–MS grade, catalog no. 533002), were supplied by Merck (Darmstadt, Germany).

Trypsin–EDTA (0.25%) (catalog no. L0932-100) and penicillin–streptomycin solution (100×) (catalog no. PS-B) were purchased from Biowest SAS (Nuaillé, France) and Capricorn Scientific GmbH (Ebsdorfergrund, Germany), respectively. Dimethyl sulfoxide (DMSO) (catalog no. 914.036) was acquired from Isolab (Eschau, Germany).

### 2.2 Cell Cultures

BV-2 microglial cells (cat. no. iCell-m011; AMS Biotechnology (Europe) Ltd., Abingdon, UK) were employed for the experiments. The cells were maintained in Dulbecco's Modified Eagle Medium (DMEM) supplemented with 10% fetal bovine serum (FBS) and 1% penicillin/streptomycin solution. Cultures were incubated at 37°C in a humidified atmosphere containing 5% $CO_2$. Sub-culturing was performed on alternate days until the cells were used for subsequent analyses.

### 2.3 Cell Viability Assay in BV-2 Microglial Cells

Cell viability was evaluated using a modified version of the MTT [3-(4,5-dimethylthiazol-2-yl)-2,5-diphenyl tetrazolium bromide] assay (Mosmann, 1983). BV-2 cells were cultured in DMEM supplemented with 10% fetal bovine serum, and 0.5% antibiotic solution.

Cell suspensions were prepared at a density of $5 \times 10^5$ cells/mL, and 100 µL aliquots were seeded into 96-well plates. The cells were incubated for 24 h at 37°C in a humidified atmosphere containing 5% $CO_2$. Following incubation, the culture medium was removed and replaced


https://doi.org/10.25135/rnp.2603.3766
Rec. Nat. Prod. 2026, 20(6):e26033766

with 100 µL of quercetin at different concentrations (1.25–10 µM). The cells were further incubated under the same conditions for 24 h to assess cytotoxicity.

At the end of the treatment period, the medium was discarded, and the cells were gently washed with 100 µL of fresh medium. Subsequently, 100 µL of fresh medium was added to each well. MTT solution (5 mg/mL) was then added at 10 µL per well, and the plates were incubated for an additional 6 h. Formazan crystals were dissolved in DMSO, and absorbance was measured at 570/620 nM.

Results were expressed as percentage viability relative to untreated controls. All experiments were performed in triplicate and repeated independently three times.

### 2.4 Determination of Nitric Oxide (NO) levels in LPS-Stimulated BV2 Cells

BV-2 microglial cells were cultured in DMEM supplemented with 10% fetal bovine serum and 0.5% antibiotic solution. Cells were maintained at 37°C in a humidified incubator with 5% $CO_2$ and subcultured every other day until use.

For nitric oxide (NO) measurements, cell suspensions were prepared at a density of $5 \times 10^5$ cells/mL and seeded into 96-well plates (100 µL per well). After 24 h of incubation, the culture medium was removed. Cells were treated with quercetin (final concentration of 1.25–10 µM) together with LPS (0.1 µg/mL) and incubated for an additional 24 h under the same conditions. For NO determination, 100 µL of supernatant was collected and mixed with an equal volume of Griess reagent containing N-(1-naphthyl) ethylenediamine dihydrochloride and sulfanilamide in water. After shaking for 5 min, the absorbance was measured at 577 nM. Quantification was performed using a sodium nitrite standard curve (sodium nitroprusside was used) (Dogan et al., 2023).

For metabolite extraction and subsequent metabolomic analysis, cells were seeded into 24-well plates under the same culture conditions and treatment protocol. After the designated incubation period, cells were processed for metabolite extraction (section 5.6.1).

### 2.5 Statistical Analysis

Cell viability data were expressed as mean ± SD. Statistical analysis was performed using one-way analysis of variance (ANOVA) followed by Dunnett's multiple comparisons test to compare each treatment group with the non-treated group (0 concentration). A p value < 0.05 was considered statistically significant (*p < 0.05 versus LPS group).

Statistical analysis of quercetin on NO production in LPS-stimulated BV2 microglial cells was performed using one-way analysis of variance (ANOVA) followed by Dunnett's multiple comparisons test, comparing each concentration with the LPS(+) group (****p < 0.0001 versus LPS group).

### 2.6 Metabolomic Analysis

#### *2.6.1 Metabolite Extraction*

Cell culture samples were rapidly quenched by removing the culture medium and washing the cells twice with ice-cold phosphate-buffered saline to eliminate extracellular metabolites, followed by immediate placement on dry ice to arrest metabolic activity. Intracellular metabolites were extracted by adding 1.0 mL of cold methanol directly onto the culture plates. Cells were thoroughly scraped, transferred into 1.5 mL microcentrifuge tubes, and incubated for 20 min at room temperature to facilitate metabolite solubilization. The extracts were vortexed for 1 min (IKA VG 3, Staufen, Germany) and clarified by protein precipitation through centrifugation at 12,000 rpm for 25 min at 4°C (Hettich Universal 320 R, Tuttlingen, Germany). Following centrifugation, 0.5 mL of the supernatant was transferred to a fresh tube and evaporated to dryness using a vacuum concentrator (Labconco CentiVap 7310030, Kansas, KA, USA). The dried extracts were reconstituted in 0.2 mL of cold acetonitrile:water (1:1, v/v), vortexed for 1 min, and centrifuged again under identical conditions to remove residual particulates. Finally, 0.1 mL of the clarified supernatant was transferred into glass vials for analysis by liquid chromatography quadrupole time-of-flight mass spectrometry (Q-TOF LC/MS).

#### *2.6.2 LC–MS Conditions*

Metabolomic analysis was performed using a Q-TOF LC/MS system (Agilent Technologies 6530, Santa Clara, CA, USA). Chromatographic separation was achieved using a reversed-phase column (Waters XBridge, 2.1 × 100 mm, 2.5 µM, Milford, MA, USA) maintained at 35°C, with a flow rate of 0.3 mL/min. The mobile phases consisted of (A) water containing 0.1% formic acid (LC/MS grade) and (B) acetonitrile containing 0.1% formic acid (LC/MS grade). The gradient elution program was as follows: 95% A at 0 min, 65% A at 2 min, 5% A at 8 min, returned to 95% A at 10 min, and held for 5 min for column re-equilibration. MS1 spectra were acquired over an m/z range of 75–1200 with randomized sample injection order to minimize batch effects. The Q-TOF mass spectrometer was operated in negative electrospray ionization (ESI) mode, capillary voltage [3.5 kV], gas temperature [325°C], drying gas flow [10 L/min], nebulizer pressure [35 psi], fragmentor voltage [175 V], and skimmer voltage [65 V]. Continuous mass axis calibration was achieved via infusion of a reference mass solution, providing lock masses at *m/z* [112.9856] and [1033.9881]. Extraction blanks were interspersed every six runs to monitor background contamination and analytical stability.

#### *2.6.3 Data Processing and Statistical Analysis*

Raw LC–MS data files were processed in MZmine 2.53. Data processing comprised mass detection, chromatogram building, peak deconvolution, isotope grouping, feature alignment, gap filling, and feature annotation by library/database matching. Mass detection was performed with a noise level of 1000. Chromatograms were built using ADAP chromatogram building with a minimum group size of 4 scans, group intensity threshold of $1.0 \times 10^3$, minimum highest intensity of $1.0 \times 10^3$, and an *m/z* tolerance of 0.008 Da (or 8 ppm). Isotopic features were grouped

with m/z tolerance 0.002 Da (or 2 ppm), an RT window of 0.05 min, and a maximum charge of 2, retaining the most intense isotope as the representative feature. Feature alignment across samples was performed with *m/z* tolerance 0.008 Da (or 8 ppm) and RT tolerance 0.05 min.

To minimize analytical background, extraction blanks were processed alongside samples, and features detected in blanks were removed prior to statistical analysis. Following preprocessing, normalized peak intensities were used for downstream statistics. Data were normalized by mean (normalization to the average peak intensity across samples) and auto-scaled (unit variance scaling); no log transformation was applied. Multivariate analysis and visualization—including PCA, PLS-DA, and heatmap clustering—were performed in MetaboAnalyst 6.0, and pathway enrichment analysis was carried out using the KEGG reference pathway library. Metabolite identification followed a two-tier strategy in accordance with Metabolomics Standards Initiative (MSI) guidelines (Sumner et al., 2007): features matching both precursor *m/z* and retention time against an in-house authentic standard library (973 metabolites) were assigned MSI Level 1 annotations, whereas features lacking direct standard matches were assigned MSI Level 2 putative annotations based on high-resolution mass accuracy and cross-database support. Differential metabolites were defined using $p < 0.05$, fold change > 1.5, and VIP > 1.0.

Statistical validation analyses were also performed to assess the robustness of the metabolomic results. The two-component PLS-DA model demonstrated acceptable-to-good model performance, with an $R^2$ value of approximately 0.90 and a $Q^2$ value of approximately 0.75, indicating adequate explanatory capacity and predictive ability. Importantly, $Q^2$ did not increase with the addition of further components, suggesting that the selected two-component model avoided unnecessary model complexity. In addition, permutation testing with 1000 randomly permuted class labels yielded a significant result ($p = 0.004$; 4/1000 permutations), supporting that the observed class separation was unlikely to have arisen by chance.

## 2.7 Molecular Docking and Molecular Dynamics Analysis

### *2.7.1 Protein Preparation and Binding Site Identification*

The three-dimensional structure of the target protein was retrieved from the Protein Data Bank (PDB ID: 3A1F) (Berman, 2000). This protein is a small, single-chain structure containing a NADPH-binding domain and does not include a co-crystallized ligand within its structure. Due to the absence of a bound ligand, identification of a potential binding site was required before the molecular docking studies. Binding site prediction was performed using the SiteMap module of the Schrödinger Suite. Although SiteMap does not define strict cut-off values for pocket evaluation, binding sites were comparatively assessed using commonly accepted parameters such as SiteScore, relative size, and volume, where higher combined values are generally considered indicative of more favorable ligand-binding regions (Halgren, 2009).

Protein preparation was carried out using the Protein Preparation Wizard implemented in Schrödinger Maestro (Schrödinger, 2023). During this process, missing hydrogen atoms were added, bond orders were assigned, and side-chain geometries were optimized. Protonation states of ionizable amino acid residues were automatically assigned under physiological conditions. Crystallographic water molecules located farther than 5 Å from the predicted binding region were removed to minimize non-essential interactions. The prepared protein structure was subsequently energy-minimized using the OPLS 2005 force field (Jorgensen et al., 1996).

### *2.7.2 Ligand Preparation and Molecular Docking Studies*

The structure of quercetin was prepared using the LigPrep module of the Schrödinger Suite (Schrödinger, 2019). As part of the ligand preparation workflow, salts and counterions were removed, and multiple plausible tautomeric forms were generated under physiological pH conditions. Generated ligand structure was subsequently energy-minimized using the conjugate gradient algorithm with the OPLS3e force field prior to molecular docking calculations.

Molecular docking studies were performed using the Glide module within the Schrödinger Maestro environment (Friesner et al., 2004). The docking grid was generated by centering on the coordinates of the most favorable binding pocket identified by SiteMap, ensuring complete coverage of the predicted active site.

For the ligand, five distinct binding poses were generated, and docking scores were calculated in terms of binding free energy (kcal/mol). The resulting poses were ranked based on their Glide docking scores, and the most favorable binding conformations were selected for subsequent molecular dynamics simulations.

### *2.7.3 Molecular Dynamics Simulations*

Molecular dynamics (MD) simulations were conducted to evaluate the stability of the protein–ligand complexes obtained from docking studies. The best-ranked binding pose of quercetin was subjected to MD simulations using the Desmond molecular dynamics engine implemented in the Schrödinger Suite (Bowers et al., 2006).

Each protein–ligand complex was solvated using the TIP3P water model in an orthorhombic simulation box, maintaining a minimum distance of approximately 10 Å between the protein surface and the box boundaries. The systems were neutralized by the addition of appropriate counterions, and physiological ionic strength was achieved by adding 0.15 M NaCl. All simulations were performed using the OPLS 2005 force field (Jorgensen et al., 1996).

Prior to the production phase, the systems were equilibrated using a standard relaxation protocol consisting of restrained energy minimization followed by short equilibration steps under NVT and NPT ensembles. Production MD simulations were carried out for 50 ns under NPT conditions at a temperature of 300 K and a pressure of 1 atm, maintained using a Nose–Hoover thermostat and a Martyna–Tobias–Klein barostat. Long-range electrostatic interactions were


https://doi.org/10.25135/rnp.2603.3766
*Rec. Nat. Prod.* 2026, 20(6):e26033766

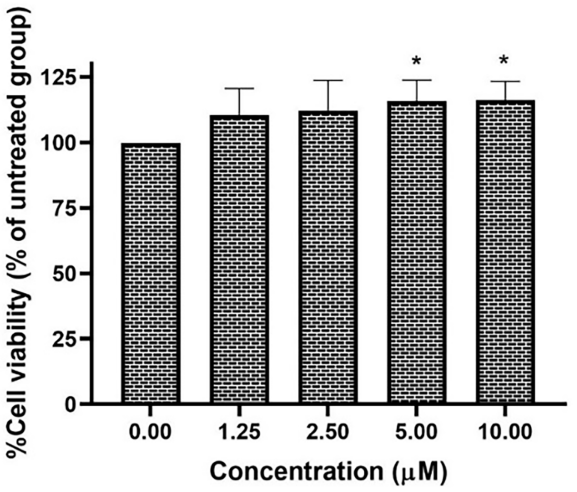


**Figure 1.** Effect of quercetin on BV-2 microglial cell viability at different concentrations (1.25–10 μM). Data are presented as mean ± SD ($n$ = 6). The untreated control group (0 μM was normalized to 100% viability. Statistical analysis was conducted using one-way analysis of variance (ANOVA) followed by Dunnett's multiple comparisons test. *p < 0.05 compared with the untreated group

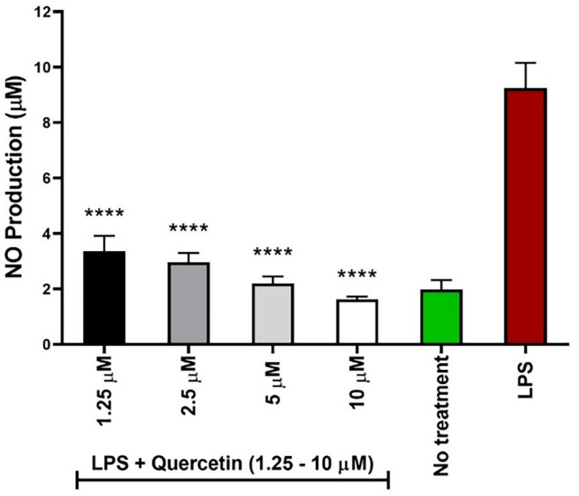


**Figure 2.** Effect of quercetin on nitric oxide (NO) production in LPS-stimulated BV-2 microglial cells. Results are presented as mean ± SD ($n$ = 6). Statistical significance was determined by one-way analysis of variance (ANOVA) followed by Dunnett's multiple comparisons test. ****p < 0.0001 compared with the LPS-treated group

treated using the particle mesh Ewald (PME) method, and a time step of 2 fs was employed throughout the simulations.

Protein stability was evaluated by calculating the RMSD of the protein backbone atoms, while residue flexibility was assessed by RMSF analysis based on Cα atoms. Ligand stability was analyzed by calculating ligand heavy-atom RMSD only during the time period in which the ligand remained within the predicted binding pocket. All trajectory analyses were performed using the Simulation Interaction Diagram and Simulation Event Analysis tools implemented in the Schrödinger Suite.

## 3 Results

### 3.1 Cell Viability Assay

As shown in Figure 1, the tested compound did not exhibit any cytotoxic effect on cell viability within the concentration range of 1.25–10 μM. Cell viability remained around or above 100% at all tested concentrations. Notably, a statistically significant increase in cell viability was observed at 5 and 10 μM compared to the untreated control group (*p < 0.05). These findings indicate that the compound is non-cytotoxic to BV-2 cells within the tested concentration range and may enhance cell proliferation at higher concentrations.

### 3.2 Inhibitory Effect of Quercetin on LPS-Induced NO Production in BV-2 Microglial Cells

As shown in Figure 2, LPS stimulation markedly increased NO production in BV-2 microglial cells compared to the untreated group. Treatment with quercetin (1.25–10 μM) significantly reduced NO levels in LPS-stimulated cells in a concentration-dependent manner. All tested concentrations of quercetin (1.25, 2.5, 5, and 10 μM) resulted in a highly significant decrease in NO production compared with the LPS-treated group (****p < 0.0001). The most pronounced suppression was observed at 10 μM, where NO levels approached those of the untreated control group. These results indicate that quercetin effectively attenuates LPS-induced NO production in BV-2 microglial cells.

### 3.3 Metabolomic Analyses

#### *3.3.1 Metabolic Profiling and Data Processing*

Untargeted LC–MS metabolomics was employed to characterize the metabolic profiles of BV2 microglia across the control (no LPS or quercetin), LPS, and LPS + quercetin groups ($n$ = 6 biological replicates per group). Unsupervised (PCA) and supervised (PLS-DA) multivariate models consistently indicated that inflammation induction (LPS group) and quercetin exposure (LPS + quercetin) were associated with distinct global metabolic phenotypes. Distinct clustering patterns indicate clear metabolic differentiation between groups. In pairwise PCA models, quercetin-treated samples were clearly separated from both reference states. For the LPS + quercetin *vs.* LPS contrast, separation was driven primarily along PC1 (39.6%), with PC2 contributing 12.7% of the explained variance, resulting in complete visual segregation (Figure 3A). A similar proportion of variance was explained in the LPS + quercetin *vs.* control group model (PC1 = 39.3%, PC2 = 12.1%) (Figure 3B). Partial least squares discriminant analysis (PLS-DA) was performed to evaluate group discrimination based on metabolomic profiles. As shown in the scores plot, a clear separation was observed among the LPS, LPS + quercetin, and control groups (Figure 4). The LPS group was distinctly separated from the control group, confirming substantial LPS-induced metabolic alterations. Notably, the control group and LPS group replicates formed compact and well-defined clusters,

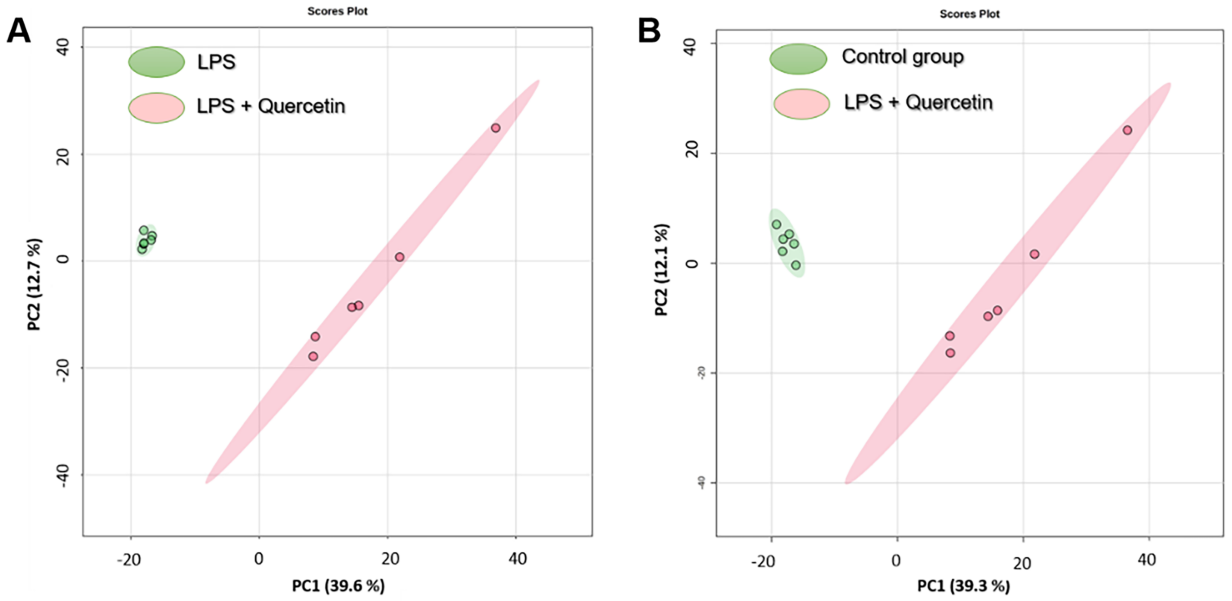


**Figure 3.** Principal component analysis (PCA) score plots showing pairwise metabolic discrimination between experimental groups. (A) PCA score plot comparing the LPS and LPS + quercetin groups. (B) PCA score plot comparing the control (no LPS or quercetin) and LPS + quercetin groups

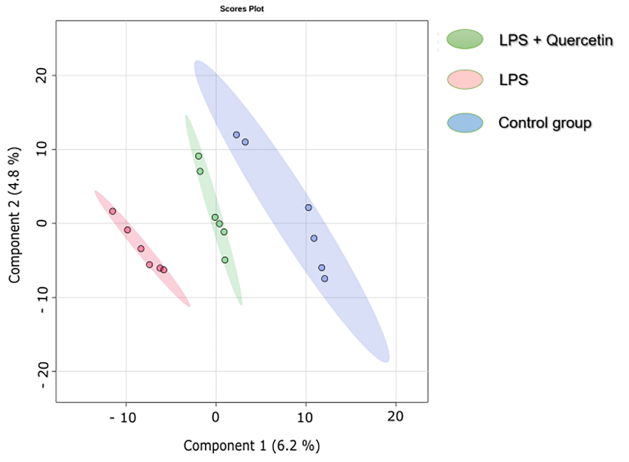


**Figure 4.** Partial least squares discriminant analysis (PLS-DA) score plot illustrating global metabolic discrimination among the LPS, LPS + quercetin, and control (no LPS or quercetin) groups

whereas the LPS + quercetin group exhibited broader dispersion, suggesting a more heterogeneous metabolic response to treatment. The quercetin-treated samples were positioned between the LPS and control groups, indicating partial modulation of the inflammatory metabolic shift. These clustering patterns were further supported by the three-class PLS-DA model, which demonstrated clear and non-overlapping group separation (Figure 4). The LPS + quercetin group formed a distinct cluster positioned between the LPS and control groups. This positioning reflects a metabolic shift away from the inflamed state toward the healthy baseline.

Metabolite-level differences were assessed to quantify specific phenotypic shifts. In the LPS + quercetin *vs.* LPS contrast, untargeted metabolomics analysis identified a total of 36 significantly altered metabolites ($p < 0.05$; VIP ≥ 1.0). Based on fold change (FC) values, the most prominently upregulated metabolites were uridine diphosphate glucose (FC = 31.1), UDP-N-acetyl-D-mannosamine (FC = 30.6), xanthine (FC = 15.7), sphingosine (FC = 13.3) and mevalonic acid (FC = 5.1) (Table 1).

In contrast, the most pronounced decreases were detected for L-xylonic acid (FC = 9.7), palmitic acid (FC = 2.7), D-tryptophan (FC = 2.2), hippuric acid (FC = 2.0), L-aspartic acid (FC = 1.9), phenylalanine (FC = 1.9), 5-hydroxyconiferyl alcohol (FC = 1.9), and adenosine monophosphate (FC = 4.4) (Table 1).

Overall, the fold change distribution indicates substantial upregulation of metabolites in nucleotide sugars and intermediates (including uridine diphosphate glucose, UDP-N-acetyl-D-mannosamine), purine/pyrimidine metabolites (xanthine, uridine), central carbon and nitrogen metabolism markers (such as gamma-aminobutyric acid (GABA), glutamic acid, and L-alanine) and sphingolipid-associated compounds, alongside moderate downregulation of selected amino acids, fatty acids, and nucleotide intermediates, reflecting a coordinated metabolic reprogramming under the studied conditions (Figure 5, Table 1).

In the LPS + quercetin *vs.* control group, a total of 23 metabolites ($p < 0.05$; VIP ≥ 1.0) were found to be significantly altered. Based on fold change (FC) values, the most prominently upregulated metabolites were uridine diphosphate glucose (FC = 39.75), pyruvic acid (FC = 6.82), cytidine (FC = 5.78), and gluconic acid (FC = 4.61).

In contrast, the most pronounced decreases were detected for L-xylonic acid (FC = 8.71) and adenosine monophosphate (AMP) (FC = 6.91). Other significantly downregulated


https://doi.org/10.25135/rnp.2603.3766
*Rec. Nat. Prod.* 2026, 20(6):e26033766

**Table 1.** Differentially altered metabolites identified in the LPS + quercetin *vs.* LPS and LPS + quercetin *vs.* control comparisons based on untargeted LC–MS metabolomics analysis (at least in one comparison; $p < 0.05$, fold change (FC) > 1.5, and VIP > 1.0). Metabolites meeting the selection criteria are presented with corresponding p values, VIP scores, fold changes, and direction of change (↑ increase, ↓ decrease). Metabolites confirmed using the in-house authentic standard library (973 compounds; matched by accurate mass and retention time) are indicated with an asterisk (*). The remaining metabolites represent putative annotations based on accurate mass

| Group | LPS + Quercetin *vs.* LPS | | | | | LPS + Quercetin *vs.* Control | | | | |
|---|---|---|---|---|---|---|---|---|---|---|
| Metabolite | p value | VIP | FDR | FC | Change | p value | VIP | FDR | FC | Change |
| 3-Hydroxy-N6,N6,N6-trimethyl-L-lysine | 0.026 | 1.1 | 0.041857 | 2.3 | ↓ | 0 | 1.45 | 0.003349 | 2.5 | ↓ |
| 3-Sulfinylpyruvic acid | 0.019 | 1.1 | 0.026724 | 2.1 | ↓ | 0.001 | 0.89 | 0.035692 | 1.29 | ↓ |
| 4-Hydroxy benzaldehyde* | 0.004 | 1.3 | 0.030883 | 3.6 | ↓ | 0.178 | 0.75 | 0.2571 | 10.71 | ↓ |
| 5-Acetamidovalerate | 0 | 1.6 | 1.76E-07 | 3.5 | ↑ | 0 | 1.64 | 7.52E-07 | 3.41 | ↑ |
| 5-Hydroxyconiferyl alcohol | 0 | 1.6 | 1.4E-05 | 1.9 | ↓ | 0 | 1.53 | 0.000212 | 1.64 | ↓ |
| Acrylic acid | 0.039 | 1 | 0.3804 | 3.9 | ↑ | 0.001 | 0.85 | 0.045213 | 1.02 | ↑ |
| Adenosine monophosphate* | 0 | 1.4 | 0.013305 | 4.4 | ↓ | 0 | 1.61 | 0.000212 | 6.91 | ↓ |
| Coproporphyrinogen III | 0.001 | 1.4 | 0.002506 | 1.6 | ↓ | 0.007 | 1.22 | 0.01315 | 1.77 | ↓ |
| Creatine | 0.001 | 1.4 | 0.00289 | 1.6 | ↑ | 0.059 | 0.89 | 0.009209 | 1.24 | ↑ |
| Cytidine* | 0.075 | <1.00 | 0.074748 | 1.82 | ↑ | 0 | 1.52 | 0.000212 | 5.78 | ↑ |
| D-Ribose | 0.196 | <1.00 | 0.006659 | 1.65 | ↑ | 0.03 | 1.05 | 0.043759 | 1.58 | ↑ |
| D-Tryptophan* | 0.045 | 1 | 0.04988 | 2.2 | ↓ | 0.187 | <1.00 | 0.10251 | 1.95 | ↓ |
| D-Xylose | 0.003 | 1.3 | 0.006659 | 1.7 | ↑ | 0.096 | <1.00 | 0.043759 | 1.58 | ↑ |
| gamma-Aminobutyric acid* | 0 | 1.4 | 0.00089 | 2.2 | ↑ | 0.002 | 1.32 | 0.007015 | 1.83 | ↑ |
| Gluconic acid* | 0.008 | 1.2 | 0.012621 | 2 | ↑ | 0 | 1.52 | 0.011666 | 4.61 | ↑ |
| Glutamic acid* | 0.001 | 1.4 | 0.00289 | 1.9 | ↑ | 0.005 | 1.27 | 0.00982 | 2.01 | ↑ |
| Glycerol 3-phosphate | 0.031 | 1 | 0.041442 | 1.6 | ↓ | 0.006 | 1.24 | 0.79049 | 2.01 | ↑ |
| Hippuric acid* | 0 | 1.5 | 0.000479 | 2 | ↓ | 0.004 | 1.28 | 0.009118 | 1.55 | ↓ |
| Hydroxypropionic acid | 0.005 | 1.2 | 0.008545 | 3.4 | ↑ | 0.171 | <1.00 | 0.021253 | 1.75 | ↑ |
| Hypoxanthine* | 0 | 1.6 | 1.4E-05 | 2 | ↑ | 0 | 1.54 | 0.000212 | 1.75 | ↑ |
| L-Alanine* | 0.047 | 1 | 0.058196 | 3.6 | ↑ | 0.121 | <1.00 | 0.63188 | 1.26 | ↑ |
| L-Aspartic acid* | 0 | 1.6 | 5.86E-05 | 1.9 | ↓ | 0 | 1.53 | 0.000212 | 2.28 | ↓ |
| L-Cysteine | 0.001 | 1.4 | 0.008823 | 2.6 | ↑ | 0.121 | <1.00 | 0.25709 | 1.17 | ↑ |
| L-Threonine* | 0.003 | 1.3 | 0.006659 | 2 | ↑ | 0.631 | <1.00 | 0.011666 | 2 | ↑ |
| L-Xylonic acid | 0 | 1.7 | 7.29E-05 | 9.7 | ↓ | 0 | 1.66 | 0.000274 | 8.71 | ↓ |
| L-Xylulose* | 0.001 | 1.4 | 0.007891 | 3 | ↑ | 0.008 | 1.21 | 0.011953 | 1.87 | ↑ |
| Mevalonic acid* | 0.035 | 1 | 0.010565 | 5.1 | ↑ | 0.452 | <1.00 | 0.007241 | 2.93 | ↑ |
| N-Methyltyramine | 0.017 | 1.1 | 0.002506 | 2.9 | ↑ | 0.015 | 1.14 | 0.002562 | 3.04 | ↑ |
| Palmitic acid | 0.03 | 1 | 0.04123 | 2.7 | ↓ | 0.1 | <1.00 | 0.1162 | 1.57 | ↓ |
| Phenylalanine* | 0.049 | 1 | 0.058986 | 1.9 | ↓ | 0.026 | 1.07 | 0.042049 | 1.84 | ↓ |
| Pipecolic acid | – | <1.00 | 0.000829 | 3.07 | ↓ | 0.013 | 1.16 | 0.02571 | 2.72 | ↓ |
| Pyruvic acid* | 0.025 | 1.07 | 0.042476 | 6.82 | ↑ | 0.114 | <1.00 | 0.042049 | 1.25 | ↑ |
| Sphingosine | 0 | 1.7 | 6.68E-11 | 13.3 | ↑ | 0.057 | <1.00 | 0 | 1.02 | ↑ |
| Thyrotropin releasing hormone | 0.013 | 1.2 | 0.019061 | 1.6 | ↑ | 0.079 | <1.00 | 0.2571 | 1.22 | ↑ |
| UDP-N-acetyl-D-mannosamine | 0.004 | 1.3 | 0.002506 | 30.6 | ↑ | 0.052 | <1.00 | 0.00323 | 27.64 | ↑ |
| Uridine* | 0 | 1.6 | 1.4E-05 | 2.3 | ↑ | 0 | 1.59 | 4.87E-05 | 2.19 | ↑ |
| Uridine diphosphate glucose | 0.002 | 1.3 | 0.0138 | 31.1 | ↑ | 0.002 | 1.35 | 0.010378 | 39.75 | ↑ |
| Xanthine | 0.008 | 1.2 | 0.000316 | 15.7 | ↑ | 0.187 | <1.00 | 0.001018 | 1.23 | ↑ |

Note: [1]FC: Fold Change, VIP: Variable importance in projection (VIP) scores, * : in house library, ($p < 0.05$, FC > 1.5, VIP > 1.0).

metabolites included pipecolic acid (FC = 2.72), 3-hydroxy-N6,N6,N6-trimethyl-L-lysine (FC = 2.50), L-aspartic acid (FC = 2.28↓), phenylalanine (FC = 1.84), and coproporphyrinogen III (FC = 1.77) (Figure 5, Table 2).

These results indicate that quercetin treatment does not merely counteract inflammation-induced metabolic alterations, but also establishes a distinct metabolic state relative to the control group. In other words, quercetin induces a metabolite profile that differs not only from inflamed cells but also from baseline physiological conditions, reflecting a treatment-specific metabolic remodeling rather than a simple restoration to the healthy state.

Heatmap-based hierarchical clustering further illustrated the distinct metabolic patterns among the experimental groups (Figure 5). The clustering pattern clearly separated inflamed samples from quercetin-treated samples, indicating a treatment-associated metabolic shift.

While thyrotropin-releasing hormone, creatine, gluconic acid, L-cysteine, L-alanine, sphingosine, and acrylic acid levels were decreased in the LPS group compared to the control group, these metabolites were markedly elevated in the LPS

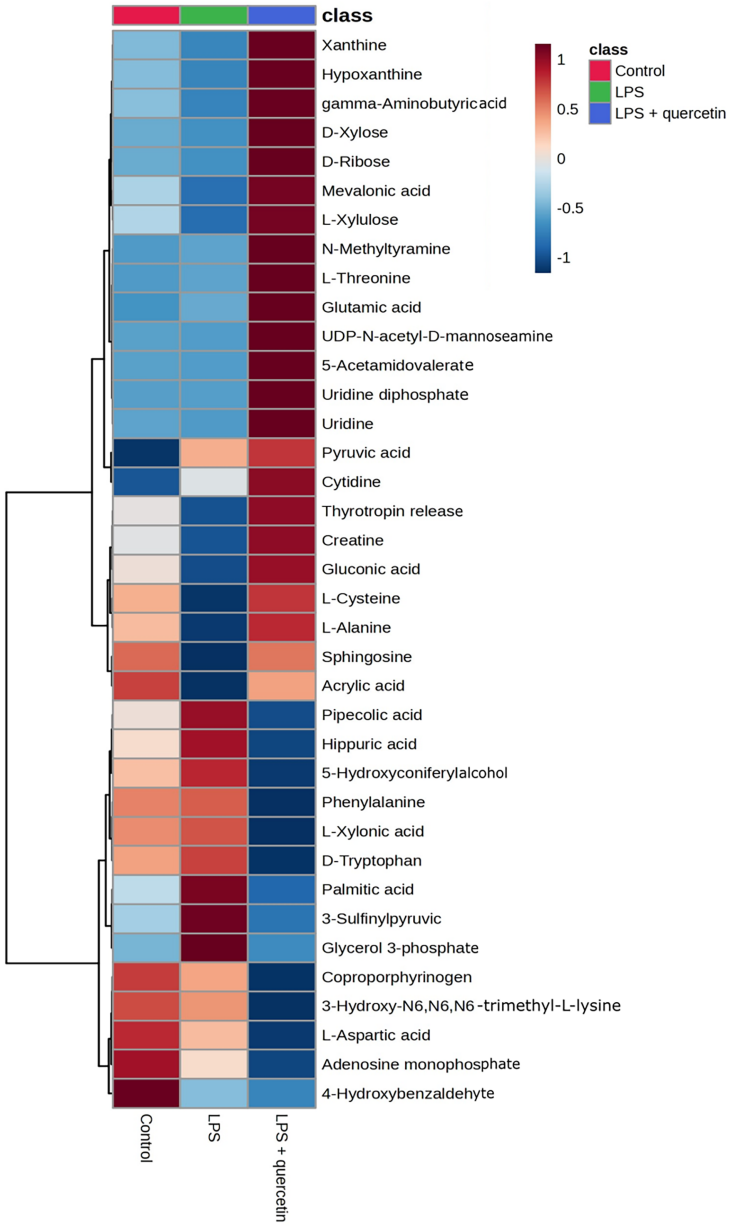


**Figure 5.** Hierarchical clustering heatmap visualization of differentially regulated metabolites among experimental groups, showing the control *vs*. LPS *vs*. LPS + quercetin comparisons. Metabolite abundances were normalized and scaled prior to visualization. Color gradients represent relative metabolite levels.

+ quercetin group, exceeding even the levels observed in the control group (Figure 5).

Conversely, pipecolic acid, hippuric acid, 5-hydroxyconiferyl alcohol, phenylalanine, L-xylonic acid, D-tryptophan, palmitic acid, and 3-sulfinylpyruvic acid levels were increased in the LPS group relative to the control group. However, following quercetin treatment, their levels declined to values lower than those detected in the control group (Figure 5).

These two opposing patterns indicate that quercetin not only suppresses inflammation-associated metabolic elevations but also restores metabolites that were reduced during inflammatory activation.

### *3.3.2 Pathway Enrichment Analysis*

Pathway enrichment analysis contextualized these shifts, highlighting a dominant effect on amino acid-centered nitrogen metabolism (Table 2). For the LPS + quercetin *vs*. LPS contrast, glutamate metabolism was significantly enriched after multiple-testing correction (6 hits; FDR = 0.047). Similarly, in the LPS + quercetin *vs*. control contrast, glutamate metabolism showed a stronger corrected signal (FDR = 0.015), supported by trend-level enrichment in the urea cycle, ammonia recycling, and aspartate metabolism (Table 2). Together, these results demonstrate that quercetin treatment induces a reproducible and coherent metabolic remodeling of BV2 cells, primarily


https://doi.org/10.25135/rnp.2603.3766
*Rec. Nat. Prod.* 2026, 20(6):e26033766

**Table 2.** Enriched metabolic pathways identified in the comparisons of LPS + quercetin *vs*. LPS and LPS + quercetin *vs*. control based on untargeted metabolomics analysis. The table summarizes significantly altered pathways, including the number of matched metabolites (hits), raw p values, and false discovery rate (FDR)–adjusted values. Only pathways meeting the threshold of FDR < 0.25 were considered for interpretation. Missing entries (–) indicate pathways that did not reach the predefined significance criteria in the respective comparison

| Group | (LPS + quercetin) *vs*. LPS | | | (LPS + quercetin) *vs*. control | | |
|---|---|---|---|---|---|---|
| Pathway | Hits | p value | FDR | Hits | p value | FDR |
| Alanine metabolism | 3 | 0.006 | 0.095 | 3 | 0.003 | 0.065 |
| Amino sugar metabolism | 2 | 0.173 | 0.745 | 3 | 0.022 | 0.192 |
| Ammonia recycling | 3 | 0.031 | 0.254 | 4 | 0.002 | 0.065 |
| Arginine and proline metabolism | 4 | 0.027 | 0.244 | 4 | 0.014 | 0.137 |
| Aspartate metabolism | 4 | 0.007 | 0.097 | 4 | 0.003 | 0.065 |
| Cysteine metabolism | 4 | 0.002 | 0.074 | 3 | 0.011 | 0.137 |
| Glucose-alanine cycle | 2 | 0.034 | 0.254 | 2 | 0.024 | 0.192 |
| Glutamate metabolism | 6 | 0.000 | 0.047 | 6 | 0.000 | 0.015 |
| Glycine and serine metabolism | 6 | 0.001 | 0.073 | 3 | 0.096 | 0.625 |
| Malate-aspartate shuttle | 2 | 0.020 | 0.211 | 2 | 0.014 | 0.137 |
| Phenylalanine and tyrosine metabolism | 3 | 0.022 | 0.211 | 3 | 0.013 | 0.137 |
| Purine metabolism | 6 | 0.005 | 0.089 | 5 | 0.009 | 0.137 |
| Urea cycle | 4 | 0.003 | 0.074 | 4 | 0.001 | 0.065 |
| Glutathione metabolism | 3 | 0.009 | 0.114 | – | – | – |
| Galactose metabolism | – | – | – | 2 | 0.160 | 0.645 |
| Gluconeogenesis | – | – | – | 2 | 0.127 | 0.645 |

involving glutamate-centered amino acid interconversion and nitrogen handling, with concurrent modulation of central carbon and nucleotide-related pools.

### 3.4 Molecular Docking Studies

Considering that the antioxidant activity of the studied ligands is hypothesized to be mediated through NADPH oxidase 2 (NOX2) inhibition, the NADPH-binding domain of this enzyme (PDB ID: 3A1F) was selected for binding site analysis. As the target protein is a small, single-chain structure lacking a co-crystallized ligand; identitifying potential binding regions was required prior to molecular docking studies.

The SiteMap results revealed three distinct binding pockets within the protein structure. These pockets were evaluated based on their SiteScore, relative size, and calculated volume, which collectively reflect pocket druggability, spatial extent, and ligand accommodation potential. Among the identified pockets, Site-1 exhibited the highest SiteScore (0.782), along with the largest relative size (42) and a volume of 92.953 Å$^3$. In comparison, Site-2 showed a lower SiteScore (0.545), a smaller relative size (19), and a volume of 44.590 Å$^3$, while Site-3 displayed a SiteScore of 0.525 with a relative size of 19 and a volume of 76.489 Å$^3$ (Table 3).

Based on the higher SiteScore and the more favorable size and volume parameters, Site-1 was considered the most suitable binding region for ligand interaction. Consequently, molecular docking and subsequent molecular dynamics simulations were performed, focusing on this pocket. The spatial locations and volumes of the identified binding pockets are illustrated in Figure 6.

**Table 3.** Identified binding pockets and their properties in the 3A1F protein

| Active sites | SiteScore | Size | Volume (Å$^3$) |
|---|---|---|---|
| **Site-1** | 0.782 | 42 | 92.953 |
| **Site-2** | 0.545 | 19 | 44.590 |
| **Site-3** | 0.525 | 19 | 76.489 |

The docking results, performed using Site 1 as the identified binding pocket revealed a binding energy of −6.28 kcal/mol for quercetin, indicating a favorable binding tendency for quercetin within the pocket. The chromen ring system of quercetin was positioned inside the cavity, whereas the dihydroxyphenyl moiety extended toward the outer region of the binding pocket, enabling additional stabilizing interactions (Figure 7A). Quercetin formed strong π–anion interactions with GLU156 and GLH184 via its hydroxyl functionalities, along with hydrogen bonds involving LEU152 and PHE186. Furthermore, electrostatic interactions with ASN182 and LYS183 were observed, accompanied by hydrophobic contacts with ILE27, CYS153, ALA159, and PHE181 (Figure 7B and C). These docking results provided the basis for subsequent molecular dynamics simulations to further evaluate the stability of the ligand–protein complexes.

### 3.5 Molecular Dynamics Studies

Molecular dynamics simulations were performed to further evaluate the stability of the quercetin–protein complex within the selected active binding pocket. Analysis of the protein backbone RMSD showed that the protein structure

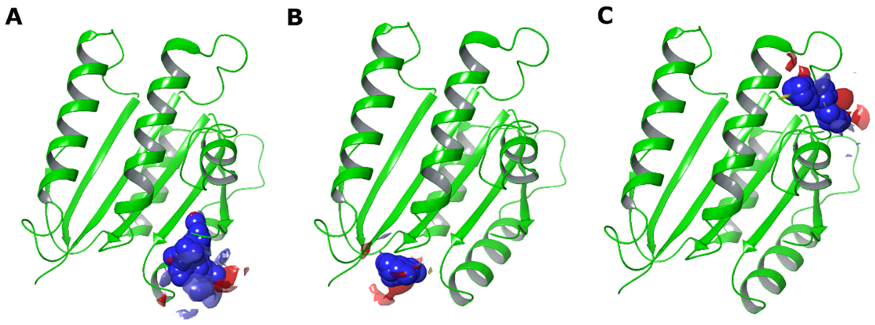


**Figure 6.** Representation of the identified active binding pockets of the 3A1F protein. Panels A–C correspond to Site-1, Site-2, and Site-3, respectively. The protein chain is shown in green, and the potential binding pockets are depicted in blue, illustrating both their spatial locations and relative volumes

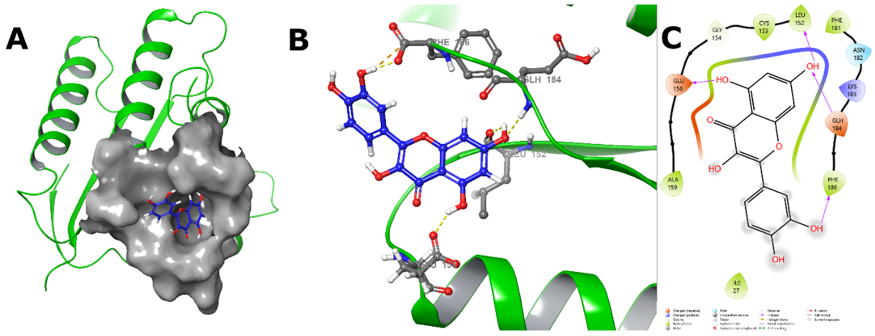


**Figure 7.** Docking pose of quercetin within the NADPH-binding domain of NADPH oxidase 2 (PDB ID: 3A1F). Panel A shows the three-dimensional representation of quercetin positioned within the active binding pocket. Panel B illustrates the 3D visualization of polar interactions formed within the active site. Panel C presents the 2D representation of all interactions occurring within the active region. Quercetin is shown in blue, interacting amino acid residues in gray, and the protein backbone in green

remained stable throughout the simulation, with RMSD values fluctuating approximately between 1.3 and 1.7 Å after an initial equilibration period, indicating preservation of the overall protein structure. Ligand RMSD calculated with ligand self-alignment fluctuated between 1.2 and 1.6 Å, demonstrating that the ligand maintained its internal conformation throughout the simulation. When RMSD was calculated relative to the protein backbone, ligand RMSD values ranged between approximately 1.6 and 2.8 Å and remained below the commonly accepted 3.0 Å stability threshold during the entire simulation, confirming that the ligand remained associated with the binding region (Figure 8A). These results indicate that the ligand did not dissociate from the pocket but underwent limited positional adjustments within the binding site.

RMSF analysis revealed that the majority of the protein backbone residues exhibited low fluctuations, with Cα RMSF values predominantly remaining below approximately 1.0 Å, indicating a generally stable protein framework during the simulation. Residues displaying RMSF values slightly above 1.0 Å showed increased local flexibility; however, these fluctuations were limited in magnitude and primarily confined to loop or solvent-exposed regions, where moderate mobility is commonly observed and does not necessarily indicate structural destabilization. Only a small number of residues reached RMSF values of approximately 2.0–2.5 Å, and these localized fluctuations did not propagate to the ligand-binding site, supporting the overall stability of the binding region throughout the simulation (Figure 8B).

Overall, the MD results support the formation of a stable macromolecule–ligand complex during the 50 ns simulation.

Interaction analysis demonstrated that quercetin formed persistent contacts with key residues within the active site. Notably, residues such as LEU152, GLU156, GLH184, ASN185, and PHE186 displayed sustained interaction frequencies over the course of the simulation. The combination of stable polar, electrostatic, and hydrophobic interactions contributed to the maintenance of quercetin within the binding pocket. Overall, the molecular dynamics results indicate that the quercetin–protein complex exhibits a stable interaction profile within accepted stability limits and are consistent with the docking-derived binding behavior. The interaction fraction results are provided in Figure 9.

## 4 Discussion

In this study, we demonstrate that quercetin suppresses LPS-induced NO production and induces a coordinated metabolic remodeling in BV-2 microglial cells. Importantly, quercetin did not merely reverse inflammatory alterations


https://doi.org/10.25135/rnp.2603.3766
*Rec. Nat. Prod.* 2026, 20(6):e26033766

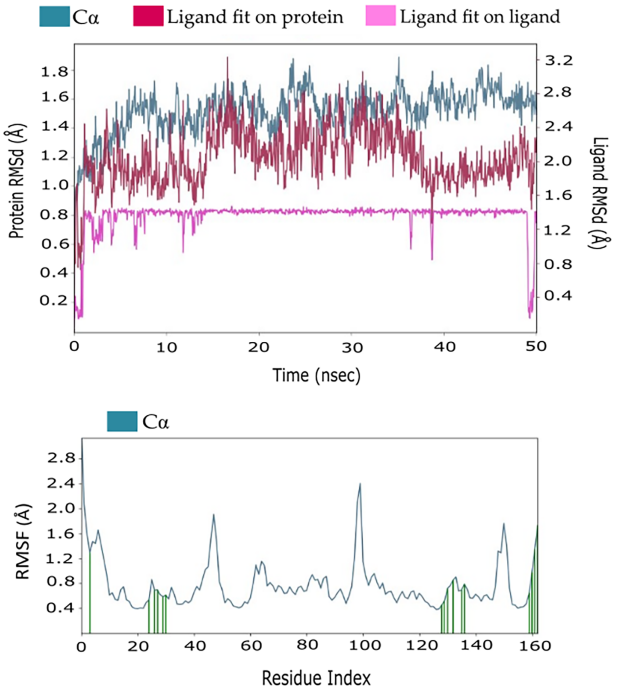


**Figure 8.** RMSD (A) and RMSF (B) plots of the molecular dynamics simulation of quercetin

but established a distinct metabolic state characterized by glutamate-centered nitrogen remodeling.

Microglial activation is strongly linked to increased iNOS expression and elevated NO production, contributing to nitrosative stress and neuronal injury under inflammatory conditions (Akiyama et al., 2000). In Alzheimer's disease (AD), iNOS levels are increased in the brain, and genetic ablation of iNOS has been shown to confer protection in experimental AD models (Heneka et al., 2015). Beyond NO generation, activated microglia also produce ROS through upregulated NOX2. In AD, the latter is rapidly stimulated by inflammatory triggers, such as Aβ, thereby connecting inflammatory signaling with cellular redox processes. Moreover, superoxide generated by NOX2 can interact with iNOS-derived NO to form peroxynitrite, further amplifying oxidative damage (Heneka et al., 2015).

NOX2 is expressed in various cell types, including endothelial cells and neurons. It is highly expressed in microglia, where it participates in immune and inflammatory responses. In animal models characterized by significant inflammation, NOX2 inhibition has been associated with the improvement of symptoms. However, whether this can be therapeutically exploited remains to be validated (Altenhöfer et al., 2012; Ma et al., 2017).

Quercetin is a flavonol characterized by two aromatic rings (A and B) connected through a three-carbon–linked pyrone ring (C) and five hydroxyl groups. Its polyphenolic structure, including the catechol moiety in the B ring, hydroxyl groups at positions 3 and 5, and the 2,3-double bond conjugated with a 4-oxo function in the C ring, is associated with its well-known antioxidant activity (Ansari et al., 2022).

The effects of quercetin on reactive oxygen species (ROS) production have likewise been directly evaluated using intracellular oxidation-based fluorescence assays. Kao et al. (2010) demonstrated that quercetin (10 μM) significantly suppressed LPS/IFN-γ-induced free radical production in DCFH-loaded BV-2 microglial cells over a 240 min observation period. In addition, Liu et al. (2013) assessed ROS production in lead (Pb)-exposed mouse brain tissue. Pb exposure increased brain ROS levels by approximately 73% compared with controls, whereas quercetin treatment (15 and 30 mg/kg/day) significantly and dose-dependently attenuated this increase ($p < 0.01$). Similarly, lipid peroxidation, measured as thiobarbituric acid reactive substances (TBARS), was elevated by approximately 75% in the Pb-treated group and was significantly reduced by quercetin administration (Liu et al., 2013).

The inhibitory effect of quercetin on iNOS expression has been directly demonstrated in several independent studies using both Western blot and RT-PCR analyses. In microglial models, quercetin has been shown to attenuate LPS- and IFN-γ-induced NO production and to downregulate iNOS transcription, an effect associated with reduced activation of NF-κB, AP-1, STAT1, and IRF-1, together with induction of heme oxygenase-1 (Chen et al., 2005). Kao et al. (2010) reported that quercetin (10 μM) reduced iNOS mRNA expression to 31.4 ± 9.1% and iNOS protein expression to 29.4 ± 7.9% of LPS/IFN-γ-stimulated BV-2 microglial cells. Similarly, Kang et al. (2013) showed that quercetin markedly reduced LPS-induced iNOS mRNA and protein expression in BV-2 microglial cells in a concentration-dependent manner. This effect was linked to inhibition of NF-κB activation through prevention of kappa Bα (IκBα) degradation (Kang et al., 2013). More recently, Hsieh et al. (2026) reported that quercetin (1–10 μM) inhibited LPS-induced iNOS protein expression in BV-2 cells by approximately 24%, 36%, and 38%, respectively, as determined by Western blot analysis (Hsieh et al., 2026). These findings are consistent with the present observation that quercetin markedly suppresses LPS-induced NO production in BV-2 microglial cells.

Beyond its anti-inflammatory actions, quercetin has also been reported to modulate mitochondrial apoptotic pathways by regulating the Bax/Bcl-2 ratio, inhibiting cytochrome c release, and suppressing caspase-3 activation and PARP-1 cleavage in the cortex and hippocampus. In experimental models, quercetin treatment has been shown to counteract LPS-induced synaptic loss and improve cognitive performance, further supporting its neuroprotective potential (Khan et al., 2018). Moreover, quercetin influences several intracellular signaling cascades, including Nrf2, MAPK, PI3K/Akt, JNK, protein kinase C, and paraoxonase-2–associated pathways, highlighting its ability to act at multiple regulatory levels (Zaplatic et al., 2019).

However, while these studies largely focus on transcriptional regulation, cytokine suppression, and apoptotic signaling, the metabolic dimension of quercetin-mediated anti-inflammatory activity remains less defined. The present metabolomic findings extend current understanding by demonstrating that quercetin-induced

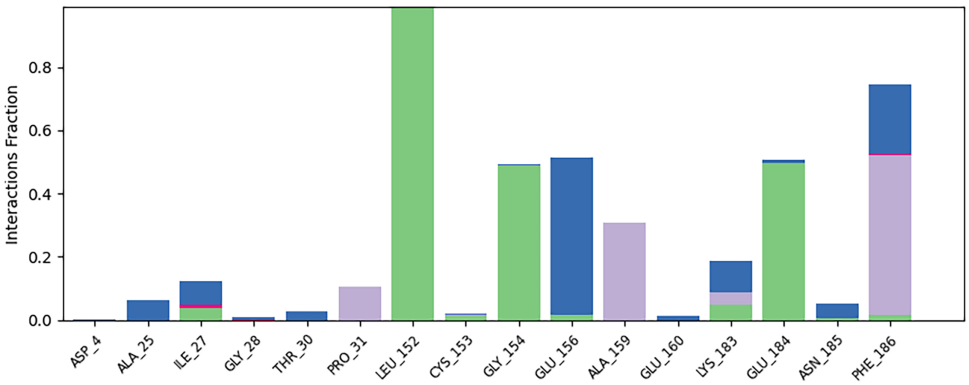


**Figure 9.** Residue-wise interaction fraction plot obtained from the molecular dynamics simulation of the quercetin–3A1F complex. The bars indicate the fraction of simulation time during which individual residues interacted with quercetin. Green represents hydrogen bonds, blue indicates hydrophobic interactions, purple corresponds to water bridges, and red denotes ionic interactions

NO suppression is accompanied by coordinated alterations in glutamate-centered amino acid metabolism, nitrogen handling pathways, and nucleotide-related intermediates. This integrative perspective suggests that the anti-inflammatory effects of quercetin are not limited to the modulation of inflammatory gene expression but are also associated with broader metabolic alterations within activated microglia.

Our LC–MS-based metabolomics study demonstrates that quercetin treatment induces a marked remodeling of the BV2 microglial metabolic phenotype under inflammatory conditions. Global separation was evident in both unsupervised (PCA) and supervised (PLS-DA) models, with the three-class PLS-DA revealing that the quercetin-treated group forms a distinct cluster positioned between the inflamed and healthy states. This distinct positioning is consistent with a partial shift away from inflammation-associated remodeling toward the healthy baseline, while simultaneously maintaining a unique, quercetin-specific metabolic signature. Such a pattern aligns with the well-described capacity of quercetin to attenuate microglial inflammatory activation through redox- and transcription-coupled mechanisms, including the suppression of pro-inflammatory signaling and the induction of cytoprotective pathways such as Nrf2/HO-1 (Kang et al., 2013; Sun et al., 2015).

Pathway enrichment analysis converged robustly on glutamate metabolism as the most prominent pathway-level signal, supported by coherent metabolite-level shifts (e.g., increased glutamate and GABA, decreased aspartate). This finding is biologically plausible given the central role of glutamatergic and GABAergic mechanisms in microglia–neuron crosstalk and neuroinflammation, where microglia both respond to and shape extracellular neurotransmitter tone and excitotoxic vulnerability (Czapski & Strosznajder, 2021). Mechanistically, microglial glutamate production is intrinsically linked to inflammatory programs and regulated by glutamine–glutamate flux. In this context, the significant enrichment of glutamate metabolism, alongside trend-level enrichment in aspartate/alanine metabolism, the urea cycle, and ammonia recycling, suggests that quercetin modulates broader nitrogen trafficking and amino-acid interconversion rather than affecting a single downstream metabolite (Haroon et al., 2016).

Furthermore, recent evidence links glutamine/glutamate metabolism directly to inflammasome biology. Modulating glutaminase-dependent glutamine metabolism has been shown to attenuate NLRP3 inflammasome activation in microglia, supporting the concept that nitrogen and carbon substrate routing acts upstream of inflammatory effector programs (Zhang et al., 2024). Given that quercetin inhibits mtROS-associated NLRP3 inflammasome activation via the promotion of mitophagy (Han et al., 2021), the glutamate-centered metabolic signature observed here likely represents a metabolic correlate of quercetin's anti-inflammatory axis, integrating mitochondrial stress control with amino-acid–linked fuel and nitrogen management.

Beyond nitrogen handling, the enrichment signal for glutathione metabolism (trend-level) is congruent with quercetin's established redox biology. In canonical BV2 models, quercetin suppresses LPS-induced NO production while activating Nrf2-dependent HO-1 induction, with MAPK pathways (e.g., ERK/p38) coordinating these transcriptional effects (Sun et al., 2015). From a metabolomics standpoint, the coordinated shift involving glutamate—a key precursor for glutathione synthesis—supports a model where quercetin exposure recalibrates the cellular balance between inflammatory oxidative stress and compensatory antioxidant capacity. While the current dataset does not directly quantify GSH/GSSG ratios, these results provide a strong rationale for targeted follow-up studies focused on glutathione redox pairs.

A notable aspect of the discriminatory metabolite panel is the coordinated alteration in central carbon endpoints. Quercetin treatment was associated with increases in lactate and pyruvate, marked changes in hexose/pentose-related metabolites (e.g., ribose/xylulose), and a strong elevation in UDP-glucose. Microglial activation is frequently linked to metabolic alterations toward glycolysis, often controlled by nutrient-sensing nodes such as mTOR/HIF-1α (Baik et al., 2019). The observed pattern suggests a


https://doi.org/10.25135/rnp.2603.3766
*Rec. Nat. Prod.* 2026, 20(6):e26033766

quercetin-associated reconfiguration of carbon partitioning in inflamed microglia. However, directionality requires cautious interpretation; increased lactate/pyruvate pools do not uniquely imply increased glycolytic flux and may alternatively reflect changes in export/uptake dynamics or mitochondrial pyruvate utilization. Nevertheless, the coherence of these carbohydrate-linked changes supports the presence of a coordinated metabolic response.

The strong signal for UDP-glucose is particularly intriguing, as UDP-sugars serve not only as biosynthetic donors for glycosylation but can also act as extracellular danger-associated signals via the P2Y14 receptor (Lazarowski & Harden, 2015). Although UDP-glucose has been studied as an inflammatory stimulus in microglia (Brautigam et al., 2008), the intracellular accumulation observed here is more conservatively interpreted as a shift in sugar nucleotide pools—potentially reflecting altered glycosylation demand—rather than direct evidence of extracellular P2Y14 engagement. Similarly, the recurrence of purine metabolism as an enriched pathway, driven by shifts in hypoxanthine, AMP, and nucleosides (uridine/cytidine), points to altered nucleotide turnover and energy salvage. Since purinergic signaling (ATP/ADP/Adenosine) is tightly interwoven with microglial activation states (Assmann et al., 2022), these shifts may reflect the bioenergetic demands of the remodeling process.

Bidirectional metabolite shifts were observed across experimental groups. Several metabolites that were reduced under inflammatory conditions—including thyrotropin-releasing hormone, creatine, L-cysteine, and sphingosine—were markedly elevated following quercetin treatment, in some cases exceeding untreated levels. Conversely, metabolites that accumulated during inflammation, such as D-tryptophan and palmitic acid were reduced after quercetin exposure to levels below baseline. This reciprocal pattern supports the concept that quercetin does not simply normalize inflammation-induced metabolic disturbances but actively reshapes the microglial metabolic landscape. Dysregulation in tryptophan metabolism is a common finding in neurological disorders (Hestad et al., 2022), and excessive intake of palmitic acid may induce neuroinflammation and possibly contribute to the development of neurodegeneration (Beaulieu et al., 2021).

Among the differentially regulated metabolites, L-cysteine, creatine, D-tryptophan, and palmitic acid have previously been reported to be associated with neuroinflammatory processes. In the present study, the levels of L-cysteine and creatine were increased following quercetin treatment compared to the inflamed group (Li et al., 2017). Sphingosine levels were also increased in the quercetin-treated group. Within the sphingolipid metabolism pathway, sphingosine can be phosphorylated to sphingosine-1-phosphate (S1P), a bioactive lipid mediator that has been associated with pro-inflammatory signaling (Zhong et al., 2019). Although no direct measurements of S1P were performed in the present study, the observed increase in sphingosine may reflect modulation at the sphingosine-to-S1P conversion step. This interpretation remains speculative and requires further experimental validation.

The integrated docking and molecular dynamics findings collectively support the favorable binding behavior of quercetin within the NADPH-binding domain of the 3A1F protein. SiteMap analysis identified Site-1 as the most druggable pocket based on its higher SiteScore, larger size, and greater volume, suggesting an appropriate structural environment for ligand accommodation. Docking results demonstrated that quercetin was favorably positioned within this cavity, forming multiple stabilizing interactions including π–anion contacts with GLU156 and GLH184, hydrogen bonds with LEU152 and PHE186, and additional electrostatic and hydrophobic interactions. Importantly, molecular dynamics simulations further confirmed the stability of this binding mode over 50 ns, as evidenced by consistently low protein backbone RMSD values and ligand RMSD values remaining within commonly accepted stability thresholds. The limited positional fluctuations of the ligand, together with stable RMSF profiles in the binding region, indicate that the interaction network observed in docking was largely preserved during dynamic conditions. Residue-wise interaction analysis revealed persistent contacts with key active-site residues, particularly LEU152, GLU156, GLH184, ASN185, and PHE186, underscoring their potential importance in ligand stabilization. Overall, these findings suggest that quercetin exhibits a stable and energetically favorable interaction profile within the selected NADPH-binding pocket.

## 5 Limitations of the Study and Conclusions

Quercetin markedly attenuated LPS-induced NO production in BV-2 microglial cells without inducing cytotoxicity within the tested micromolar range, and this anti-inflammatory effect was accompanied by coherent remodeling of the microglial metabolic phenotype. Multivariate and pathway analyses indicated that quercetin shifted the inflamed metabolome toward the untreated baseline while maintaining a distinct treatment-associated metabolic signature dominated by alterations in glutamate metabolism. Taken together, these findings indicate that quercetin-mediated suppression of inflammatory signaling in activated microglia was associated with coordinated metabolic alterations involving redox-related processes, nitrogen handling, and central carbon metabolism. In parallel, in silico analyses suggested that quercetin can stably interact with the NADPH binding domain of NOX2 (PDB ID: 3A1F), providing a structural framework that may contribute to its observed anti-inflammatory and metabolic effects. Future studies incorporating targeted validation and flux-oriented assays in primary microglia and in vivo models will be essential to define causal mechanisms and to determine the translational relevance of the identified metabolic signatures.

Several methodological considerations should be acknowledged when interpreting the present metabolomic findings. Untargeted analyses were conducted exclusively in negative ESI mode, which may have limited coverage of metabolite classes that ionize preferentially in positive mode, such as

certain amines and lipid species. Dual-polarity acquisition in future studies could further expand the metabolic landscape captured (Yu et al., 2022).

Metabolite identification relied on accurate mass and retention time matching, including comparisons with an in-house authentic standard library, but MS/MS fragmentation data were not acquired in the present workflow. While this approach provides a solid basis for putative annotation, confirmation by targeted MS/MS or orthogonal methods would strengthen individual identifications in accordance with Metabolomics Standards Initiative (MSI) guidelines (Sumner et al., 2007).

It should also be noted that several discriminatory metabolites eluted at or near the chromatographic void volume on the reversed-phase column, where chromatographic resolution is inherently reduced. Although these features were consistently detected across replicates and passed quality filtering, identifications in this retention time region should be interpreted with appropriate caution. Similarly, a small number of less common adduct forms were assigned during annotation, which may warrant additional verification. Furthermore, while the untargeted metabolomic approach provided a comprehensive overview of metabolic alterations, independent targeted validation of the identified metabolites was not performed and remains an important objective for future studies.

Although direct measurements of ROS production and iNOS/NOX2 expression were not performed in the present study, the potential involvement of these pathways was discussed in the context of previous experimental studies reporting similar effects of quercetin. Therefore, the proposed mechanistic interpretations should be considered literature-supported hypotheses rather than direct experimental evidence from the current study.

Finally, the present study relied exclusively on the immortalized BV-2 microglial cell line, which may not fully reproduce the biological complexity and phenotypic heterogeneity of primary microglia. Therefore, validation in primary microglial cultures and in vivo neuroinflammatory models will be important to confirm the reproducibility and translational relevance of the observed metabolic alterations.

## Acknowledgement

During the preparation of this work the authors used ChatGPT 5.2 in order to text editing. After using this tool, the authors reviewed and edited the content as needed and take full responsibility for the content of the published article.

## Funding Statement

This research did not receive any specific grant from funding agencies in the public, commercial, or not-for-profit sectors.

## Author Contributions

Conceptualization; VMK, AA, OK, and V.S.; methodology, VMK, AA, OK, and MC; software, VMK, AA, OK, EK and MC; validation, VMK, AA, OK, EK and MC; formal analysis, VMK, OK, AA, MÇ, and V.S.; investigation, VMK, AA, OK, and V.S.; resources, VMK, OK and MC; data curation, VMK, AA, OK, EK, and V.S.; writing—original draft preparation, VMK, AA, and OK; writing—review and editing; VMK, AA, OK, MC and V.S.; visualization, VMK, AA, OK, and EK; project administration, VMK, AA, OK, MC and V.S.; Supervision, VMK, AA, OK, MC and V.S. All authors have read and agreed to the published version of the manuscript.

## Availability of Data and Materials

The authors declare that should any raw data files be needed about the further data of the study, they are available from the corresponding author upon reasonable request. Source data are provided with this paper.

## Conflicts of Interest

The authors declare that they do not have any conflict of interest.

## ORCID

Vahap Murat Kutluay: 0000-0003-4135-3497
Ahmet Avcı: 0000-0001-7429-9349
Emine Koç: 0000-0003-3122-7104
Mustafa Çelebier: 0000-0001-7712-5512
Veronique Seidel: 0000-0003-3880-5261
Ozan Kaplan: 0000-0001-7429-9349

## References

Akiyama, H., Barger, S., Barnum, S., Bradt, B., Bauer, J., Cole, G. M., Cooper, N. R., Eikelenboom, P., Emmerling, M., Fiebich, B. L., Finch, C. E., Frautschy, S., Griffin, W. S., Hampel, H., Hull, M., Landreth, G., Lue, L., Mrak, R., Mackenzie, I. R., McGeer, P. L. et al. (2000). Inflammation and Alzheimer's disease. *Neurobiology of Aging*, *21*(3), 383–421. DOI: 10.1016/s0197-4580(00)00124-x.

Altenhöfer, S., Kleikers, P. W. M., Radermacher, K. A., Scheurer, P., Rob Hermans, J. J., Schiffers, P., Ho, H., Wingler, K. & Schmidt, H. H. H. W. (2012). The NOX toolbox: Validating the role of NADPH oxidases in physiology and disease. *Cellular and Molecular Life Sciences*, *69*(14), 2327–2343. DOI: 10.1007/s00018-012-1010-9.

Ansari, P., Choudhury, S. T., Seidel, V., Rahman, A. B., Aziz, M. A., Richi, A. E., Rahman, A., Jafrin, U. H., Hannan, J. M. A. & Abdel-Wahab, Y. H. A. (2022). Therapeutic potential of quercetin in the management of type-2 diabetes mellitus. *Life*, *12*(8), 1146. DOI: 10.3390/life12081146.

Anwar, A., Yameen, D., Masood, M., Parvez, S. & Haque, M. M. (2025). Neuronal Nitric Oxide Synthase (nNOS) uncoupling in ischemic stroke: Mechanisms of oxidative/nitrosative stress and opportunities for neuroprotection: A review. *International Journal of Biological Macromolecules*, *332*, 148589. DOI: 10.1016/j.ijbiomac.2025.148589.

Assmann, C. E., Apolloni, S., Ignácio, Z. M. & Bagatini, M. D. (2022). Editorial: Purinergic signaling and neuroinflammation.

*Frontiers in Pharmacology*, *13*, 94. DOI: 10.3389/fphar.2022.1113063.

Baik, S. H., Kang, S., Lee, W., Choi, H., Chung, S., Kim, J.-I. & Mook-Jung, I. (2019). A breakdown in metabolic reprogramming causes microglia dysfunction in Alzheimer's disease. *Cell Metabolism*, *30*(3), 493–507.e496. DOI: 10.1016/j.cmet.2019.06.005.

Beaulieu, J., Costa, G., Renaud, J., Moitié, A., Glémet, H., Sergi, D. & Martinoli, M. G. (2021). The neuroinflammatory and neurotoxic potential of palmitic acid is mitigated by oleic acid in microglial cells and microglial-neuronal co-cultures. *Molecular Neurobiology*, *58*(6), 3000–3014. DOI: 10.1007/s12035-021-02328-7.

Berman, H. M. (2000). The protein data bank. *Nucleic Acids Research*, *28*(1), 235–242. DOI: 10.1093/nar/28.1.235.

Bowers, K. J., Sacerdoti, F. D., Salmon, J. K., Shan, Y., Shaw, D. E., Chow, E., Xu, H., Dror, R. O., Eastwood, M. P., Gregersen, B. A., Klepeis, J. L., Kolossvary, I. & Moraes, M. A. (2006). Molecular dynamics—scalable algorithms for molecular dynamics simulations on commodity clusters. SC '06: Proceedings of the 2006 ACM/IEEE Conference on Supercomputing, Tampa, FL, USA (pp. 43). DOI: 10.1109/SC.2006.54.

Brautigam, V. M., Dubyak, G. R., Crain, J. M. & Watters, J. J. (2008). The inflammatory effects of UDP-glucose in N9 microglia are not mediated by P2Y14 receptor activation. *Purinergic Signalling*, *4*(1), 73–78. DOI: 10.1007/s11302-008-9095-1.

Chen, J. C., Ho, F. M., Chao, P. D. L., Chen, C. P., Jeng, K. C. G., Hsu, H. B., Lee, S. T., Wu, W. T. & Lin, W. W. (2005). Inhibition of iNOS gene expression by quercetin is mediated by the inhibition of IκB kinase, nuclear factor-kappa B and STAT1, and depends on heme oxygenase-1 induction in mouse BV-2 microglia. *European Journal of Pharmacology*, *521*(1–3), 9–20. DOI: 10.1016/j.ejphar.2005.08.005.

Cheng, J., Zhang, R., Xu, Z., Ke, Y., Sun, R., Yang, H., Zhang, X., Zhen, X. & Zheng, L.-T. (2021). Early glycolytic reprogramming controls microglial inflammatory activation. *Journal of Neuroinflammation*, *18*(1), 129. DOI: 10.1186/s12974-021-02187-y.

Czapski, G. A. & Strosznajder, J. B. (2021). Glutamate and GABA in microglia-neuron cross-talk in Alzheimer's disease. *International Journal of Molecular Sciences*, *22*(21), 11677. DOI: 10.3390/ijms222111677.

Dogan, Z., Kutluay, V. M., Genc, Y. & Saracoglu, I. (2023). Interactions between phenolic constituents of and key targets associated with inflammation: Network pharmacology, molecular docking analysis and assays. *Journal of Biomolecular Structure & Dynamics*, *41*(4), 1281–1294. DOI: 10.1080/07391102.2021.2019119.

Friesner, R. A., Banks, J. L., Murphy, R. B., Halgren, T. A., Klicic, J. J., Mainz, D. T., Repasky, M. P., Knoll, E. H., Shelley, M., Perry, J. K., Shaw, D. E., Francis, P. & Shenkin, P. S. (2004). Glide: A new approach for rapid, accurate docking and scoring. 1. Method and assessment of docking accuracy. *Journal of Medicinal Chemistry*, *47*(7), 1739–1749. DOI: 10.1021/jm0306430.

Halgren, T. A. (2009). Identifying and characterizing binding sites and assessing druggability. *Journal of Chemical Information and Modeling*, *49*(2), 377–389. DOI: 10.1021/ci800324m.

Han, X., Xu, T., Fang, Q., Zhang, H., Yue, L., Hu, G. & Sun, L. (2021). Quercetin hinders microglial activation to alleviate neurotoxicity via the interplay between NLRP3 inflammasome and mitophagy. *Redox Biology*, *44*, 102010. DOI: 10.1016/j.redox.2021.102010.

Haroon, E., Miller, A. H. & Sanacora, G. (2016). Inflammation, glutamate, and glia: A trio of trouble in mood disorders. *Neuropsychopharmacology*, *42*(1), 193–215. DOI: 10.1038/npp.2016.199.

Heneka, M. T., Carson, M. J., El Khoury, J., Landreth, G. E., Brosseron, F., Feinstein, D. L., Jacobs, A. H., Wyss-Coray, T., Vitorica, J., Ransohoff, R. M., Herrup, K., Frautschy, S. A., Finsen, B., Brown, G. C., Verkhratsky, A., Yamanaka, K., Koistinaho, J., Latz, E., Halle, A., Petzold, G. C. et al. (2015). Neuroinflammation in Alzheimer's disease. *The Lancet Neurology*, *14*(4), 388–405. DOI: 10.1016/s1474-4422(15)70016-5.

Heneka, M. T., van der Flier, W. M., Jessen, F., Hoozemanns, J., Thal, D. R., Boche, D., Brosseron, F., Teunissen, C., Zetterberg, H., Jacobs, A. H., Edison, P., Ramirez, A., Cruchaga, C., Lambert, J.-C., Laza, A. R., Sanchez-Mut, J. V., Fischer, A., Castro-Gomez, S., Stein, T. D., Kleineidam, L. et al. (2025). Neuroinflammation in Alzheimer disease. *Nature Reviews Immunology*, *25*(5), 321–352. DOI: 10.1038/s41577-024-01104-7.

Hestad, K., Alexander, J., Rootwelt, H. & Aaseth, J. O. (2022). The role of tryptophan dysmetabolism and quinolinic acid in depressive and neurodegenerative diseases. *Biomolecules*, *12*(7), 998. DOI: 10.3390/biom12070998.

Hsieh, C. Y., Chuang, C. H., Gomez, M. C., Tayo, L. L., Huang, S. M. & Tsai, P. W. (2026). Computational analysis and verification insights into quercetin's suppression of neuroinflammation in BV2 microglia through NF-κB pathway inhibition. *Current Medicinal Chemistry*, *33*, 3089–3106. DOI: 10.2174/0109298673395813250901012530.

Jorgensen, W. L., Maxwell, D. S. & Tirado-Rives, J. (1996). Development and testing of the OPLS all-atom force field on conformational energetics and properties of organic liquids. *Journal of the American Chemical Society*, *118*(45), 11225–11236. DOI: 10.1021/ja9621760.

Kamila, P., Kar, K., Chowdhury, S., Chakraborty, P., Dutta, R., Sowmiya, S., Singh, S. A. & Prajapati, B. G. (2025). Effect of neuroinflammation on the progression of Alzheimer's disease and its significant ramifications for novel anti-inflammatory treatments. *IBRO Neuroscience Reports*, *18*, 771–782. DOI: 10.1016/j.ibneur.2025.05.005.

Kang, C. H., Choi, Y. H., Moon, S. K., Kim, W. J. & Kim, G. Y. (2013). Quercetin inhibits lipopolysaccharide-induced nitric oxide production in BV2 microglial cells by suppressing the NF-κB pathway and activating the Nrf2-dependent HO-1 pathway. *International Immunopharmacology*, *17*(3), 808–813. DOI: 10.1016/j.intimp.2013.09.009.

Kao, T. K., Ou, Y. C., Raung, S. L., Lai, C. Y., Liao, S. L. & Chen, C. J. (2010). Inhibition of nitric oxide production by quercetin in endotoxin/cytokine-stimulated microglia. *Life Sciences*, *86*(9–10), 315–321. DOI: 10.1016/j.lfs.2009.12.014.

Khan, A., Ali, T., Rehman, S. U., Khan, M. S., Alam, S. I., Ikram, M., Muhammad, T., Saeed, K., Badshah, H. & Kim, M. O. (2018). Neuroprotective effect of quercetin against the detrimental effects of LPS in the adult mouse brain [Original Research]. *Frontiers in Pharmacology*, *9*, 2269. DOI: 10.3389/fphar.2018.01383.

Kwon, H. S. & Koh, S.-H. (2020). Neuroinflammation in neurodegenerative disorders: The roles of microglia and astrocytes. *Translational Neurodegeneration*, *9*(1), 42. DOI: 10.1186/s40035-020-00221-2.

Lazarowski, E. R. & Harden, T. K. (2015). UDP-sugars as extracellular signaling molecules: Cellular and physiologic consequences of P2Y14 receptor activation. *Molecular Pharmacology*, *88*(1), 151–160. DOI: 10.1124/mol.115.098756.

Li, T., Wang, L., Hu, Q., Liu, S., Bai, X., Xie, Y., Zhang, T., Bo, S., Gao, X., Wu, S., Li, G. & Wang, Z. (2017).

Neuroprotective roles of l-cysteine in attenuating early brain injury and improving synaptic density via the CBS/H2S pathway following subarachnoid hemorrhage in rats [Original Research]. *Frontiers in Neurology*, *8*, 176. DOI: 10.3389/fneur.2017.00176.

Liu, C. M., Zheng, G. H., Cheng, C. & Sun, J. M. (2013). Quercetin protects mouse brain against lead-induced neurotoxicity. *Journal of Agricultural and Food Chemistry*, *61*(31), 7630–7635. DOI: 10.1021/jf303387d.

Ma, M. W., Wang, J., Zhang, Q., Wang, R., Dhandapani, K. M., Vadlamudi, R. K. & Brann, D. W. (2017). NADPH oxidase in brain injury and neurodegenerative disorders. *Molecular Neurodegeneration*, *12*(1), 7. DOI: 10.1186/s13024-017-0150-7.

Mosmann, T. (1983). Rapid colorimetric assay for cellular growth and survival: Application to proliferation and cytotoxicity assays. *Journal of Immunological Methods*, *65*(1–2), 55–63. DOI: 10.1016/0022-1759(83)90303-4.

Peng, B., Li, H. & Peng, X. X. (2015). Functional metabolomics: From biomarker discovery to metabolome reprogramming. *Protein & Cell*, *6*(9), 628–637. DOI: 10.1007/s13238-015-0185-x.

Schrödinger, L. L. C. (2019). *LigPrep, Schrödinger Release 2019-4*, New York, NY, USA: Schrödinger.

Schrödinger, L. L. C. (2023). *Maestro, Schrödinger Release 2023-4*, New York, NY, USA: Schrödinger.

Singh, D. (2022). Astrocytic and microglial cells as the modulators of neuroinflammation in Alzheimer's disease. *Journal of Neuroinflammation*, *19*(1), 206. DOI: 10.1186/s12974-022-02565-0.

Sumner, L. W., Amberg, A., Barrett, D., Beale, M. H., Beger, R., Daykin, C. A., Fan, T. W., Fiehn, O., Goodacre, R., Griffin, J. L., Hankemeier, T., Hardy, N., Harnly, J., Higashi, R., Kopka, J., Lane, A. N., Lindon, J. C., Marriott, P., Nicholls, A. W., Viant, M. R. et al. (2007). Proposed minimum reporting standards for chemical analysis Chemical Analysis Working Group (CAWG) Metabolomics Standards Initiative (MSI). *Metabolomics*, *3*(3), 211–221. DOI: 10.1007/s11306-007-0082-2.

Sun, G. Y., Chen, Z. H., Jasmer, K. J., Chuang, D. Y., Gu, Z. Z., Hannink, M. & Simonyi, A. (2015). Quercetin attenuates inflammatory responses in BV-2 microglial cells: Role of MAPKs on the Nrf2 pathway and induction of heme oxygenase-1. *PLoS One*, *10*, e0141509. DOI: 10.1371/journal.pone.0141509.

Yu, M., Dolios, G. & Petrick, L. (2022). Reproducible untargeted metabolomics workflow for exhaustive MS2 data acquisition of MS1 features. *Journal of Cheminformatics*, *14*(1), 6. DOI: 10.1186/s13321-022-00586-8.

Zaplatic, E., Bule, M., Shah, S. Z. A., Uddin, M. S. & Niaz, K. (2019). Molecular mechanisms underlying protective role of quercetin in attenuating Alzheimer's disease. *Life Sciences*, *224*(8), 109–119. DOI: 10.1016/j.lfs.2019.03.055.

Zhang, Z., Li, M., Li, X., Feng, Z., Luo, G., Wang, Y. & Gao, X. (2024). Glutamine metabolism modulates microglial NLRP3 inflammasome activity through mitophagy in Alzheimer's disease. *Journal of Neuroinflammation*, *21*(1), 261. DOI: 10.1186/s12974-024-03254-w.

Zhong, L. S., Jiang, X., Zhu, Z. H., Qin, H. Y., Dinkins, M. B., Kong, J. N., Leanhart, S., Wang, R., Elsherbini, A., Bieberich, E., Zhao, Y. J. & Wang, G. H. (2019). Lipid transporter Spns2 promotes microglia pro-inflammatory activation in response to amyloid-beta peptide. *Glia*, *67*(3), 498–511. DOI: 10.1002/glia.23558.